Engineering Analysis with Boundary Elements 35 (2011) 1181–1189

Contents lists available at ScienceDirect

Engineering Analysis with Boundary Elements

journal homepage: www.elsevier.com/locate/enganabound

A novel boundary element approach for solving the anisotropic potential problems

Y.M. Zhang [a,b,*], Z.Y. Liu [a], J.T. Chen [c], Y. Gu [d]

[a] Institute of Applied Mathematics, Shandong University of Technology, Zibo 255049, Shandong Province, PR China
[b] State Key Laboratory of Structural Analysis for Industrial Equipment, Dalian University of Technology, Dalian 116024, PR China
[c] Department of Harbor and River Engineering, National Taiwan Ocean University, Keelung 20224, Taiwan
[d] Center for Numerical Simulation Software in Engineering and Sciences, Department of Engineering Mechanics, Hohai University, Nanjing 210098, PR China

ARTICLE INFO

Article history:
Received 18 January 2011
Accepted 17 May 2011

Keywords:
BEM
Anisotropic
Potential problems
IBIE
Nonsingular IBIE

ABSTRACT

This presentation is mainly devoted to the research on the regularization of indirect boundary integral equations (IBIEs) for anisotropic potential problems. Based on a new idea, a novel regularization technique is pursued, in which the regularized IBIEs excluding the CPV and HFP integrals are established. The proposed method has many advantages. First, it does not need to calculate multiple integral as the Galerkin method, so it is simple and easy for programming. Second, it can compute boundary quantities $\partial u/\partial x_i$ ($i=1,2$). Third, the anisotropic problems can be solved directly without transforming them into isotropic ones so that no inverse transform is required. Finally, the gradient BIEs are independent of the potential BIEs and they can provide variously useful equations. Numerical examples show that a better precision and high computational efficiency can be achieved by the present method.

1. Introduction

Anisotropic media always occur in nature, such as woods, crystals and sedimentary rocks, and can also be produced artificially, such as laminated and fiber-reinforced construction and electronic materials, cables, cylinders and tubes. Increase in the use of these materials in structural applications has considerably renewed the interest in the solutions to potential problems in anisotropy. Generally, the anisotropic potential problems include the problem of heat conduction in anisotropic media, the problem of subsurface flow in anisotropic media, and the problem of torsion in anisotropic uniform bar.

It is well known that the numerical analysis for anisotropic problems has been performed by utilizing experimental, analytical and numerical methods. The usual numerical method such as the finite difference method (FDM), finite element method (FEM), boundary element method (BEM), and meshfree method can be applied to solve such problem. The FEM has long been a dominant numerical technique in the simulation of many industrial problems. However, this method requires discretizing the whole computational domain, which is often computational costly and sometimes mathematically troublesome for some complex problems. For solving the infinite domain problems, the FEM needs to truncate infinite domain into an artificial finite region with subtle artificial boundary conditions or absorbing layers. This truncation can be somewhat arbitrary largely based on various trial-error or empirical approaches. As a domain discretization technique, the FEM is also less effective for inverse problems in which measurement is often only accessible on the boundary. As an alternative approach, the BEM has long been claimed to avoid such drawbacks [1–4]. It is well known that the BEM can reduce the discretization complexity by one dimension compared to that of the FEM. It is also worth noting that the derivatives of the physical quantity can be calculated directly from the original boundary integral equations, so that the solution accuracy of both the physical quantities and its derivatives has the same orders of magnitude. In sharp contrast, the domain-type numerical methods, such as the FEM, do not have such good property.

As the price pays for such merits, the standard BEM formulation, however, has to evaluate varied orders of singular integrals, which requires great care and significant analysis. In the past decades, tremendous effort was devoted to derive convenient integral forms or sophisticated computational techniques for calculating the troublesome singular integrals. These proposed methods can be summarized on the whole as two categories: the local and the global strategies. The local strategies are employed to calculate the singular integrals directly. They usually include,

* Corresponding author at: Institute of Applied Mathematics, Shandong University of Technology, Zibo 255049, PR China.
E-mail address: zymfc@163.com (Y.M. Zhang).

0955-7997/$ - see front matter © 2011 Elsevier Ltd. All rights reserved.
doi:10.1016/j.enganabound.2011.05.007

but are not limited to, analytical and semi-analytical one [5,6], new Gaussian quadrature [7], the local regularization method [8,9], transformation method [10–12], finite-part integral [13,14], subtraction technique [15,16], etc. It is worth noting that the subtraction technique proposed in Refs. [15,16] requires an auxiliary boundary in the desingularization processes. This method converts the singular integrals on the real boundary into the auxiliary boundary and calculates the singular integrals on auxiliary boundary directly. Although the geometric shapes of the selected auxiliary boundary are always regular, it also requires a lot of complex derivation and numerical calculation. If the number of boundary nodes increases, the procedure would require much processing and CPU time because each nodes requires an auxiliary boundary. The analytical algorithm needs enormous works of deduction and is generally considered more difficult for curved elements. The coordinate transformation method, which is invalid to the strongly and hyper-singular integrals, is merely utilized to treat weakly singularities. Among these methods, the local regularization technique proposed by Guiggiani et al. [17,18] is extensively used to handle various orders of singularities. The main drawback of this technique [19,20] is that it requires the expansion of every quantity involved in the integrand as Taylor's series about the local distance. The global strategies are mainly adopted to calculate the singular integrals indirectly, such as the method of fundamental solution or the virtual BEM [21,22], the null field method [23–25], the simple solution method [26,27], etc.

Up to now, many attempts have also appeared in the open literature to deal with the anisotropic potential problems. The representative methods to solve such problems are to transform them into isotropic ones or to use the Galerkin BEM. Hu [28] converted the torsion problem of anisotropic bar into the relevant isotropic problem by coordinate conversion method. Rungamornrat et al. [29,30] presented a weakly singular, symmetric Galerkin boundary element method to analyze the anisotropic Darcy's flow problems. The key step in this regularization procedure is to construct the special decompositions for the fluid velocity fundamental solution and the strongly singular kernel which are well-suited for integration by parts via Stokes' theorem. As demonstrated in the numerical experiment, this method is proved to be accurate and efficient even when relatively coarse meshes are employed. Wang [31] derived a new traction integral equation involving only CPV singularities which can be solved directly, and no hyper-singular terms. Mera et al. [32,33] numerically implemented the BEM to solve steady state anisotropic heat conduction problems. Wu et al. [34] developed a generalized boundary integral formulation and applied it for the analysis of seepage flow through the soil media. Brebbia and Chang [35] utilized the BEM to deal with seepage problems in zoned anisotropic soils. Dumir and Kumar [36] proposed a complex variable boundary element method for solving the torsion of anisotropic cylindrical/prismatic bars. Chen et al. [37] used dual BEM to solve seepage problem with sheetpiles.

The efficient elimination of singularities, which is even more difficult than the cases in isotropy, is also a key point when using the BEM to solve the anisotropic potential problems. In this paper, a novel regularization technique is pursued, in which the regularized indirect BIE is established. Compared with the existing methods, the presentation has many advantages. First, it can deal with problems directly without transforming them into isotropic ones, and for this reason, no inverse transform is required. Second, this method does not require to calculate multiple integrals as the Galerkin method, and evaluate CPV integrals indirectly, and so it is simple and easy for programming. Third, the proposed gradient BIEs are independent of the potential BIEs and, as such, can be collocated at the same locations as the potential BIEs. This provides additional and concurrently useful equations for various purposes. Finally, it is suited for the computation of $\partial u/\partial x_i$ $(i=1,2)$ on the boundary, not only limited to normal flux $\partial u/\partial n$.

In the numerical implementation, the boundary geometry is depicted by both quadratic Lagrange's and exact elements. Among these elements the quadratic elements are the most representative, by which a numerically systematic scheme is established. Besides, in engineering applications, the structures with circle or ellipse boundaries are widely used in order to avoid stress concentrations around sharp corners. The exact elements are proposed so that the error of the results will arise mainly from the approximation of boundary quantities.

In order to show the extensive applicability and validity of the proposed algorithm, we apply this method to solve all the above-mentioned three problems of the anisotropic potential problems. Example 1 and example 2 consider two heat conduction problems with multi-connected bounded domains in anisotropic media, and especially calculate the isotherms in various temperature fields. Example 3 studies the torsion problem of anisotropic uniform bar, in which the calculation of shear stresses associated with the gradient BIEs is a significant and difficult problem, since it has to deal with $\partial u/\partial x_i$ $(i=1,2)$ instead of $\partial u/\partial n$. Furthermore, in example 4 the seepage flow in anisotropic media is considered. The pressure distribution on the dam base and the equipotential lines at various points under the dam are analyzed in this example. It is shown that a better precision and high computational efficiency can be achieved by the present method.

2. Basic theorems

In this paper, we always assume that Ω is a bounded domain in R^2, Ω_c its open complement, and $\Gamma=\partial\Omega$ their common boundary. $\boldsymbol{t}(\boldsymbol{x})$ and $\boldsymbol{n}(\boldsymbol{x})$(or $\boldsymbol{t}$ and $\boldsymbol{n}$) are the unit tangent and outward normal vectors of Γ to the domain Ω at the point $\boldsymbol{x}$, respectively. Assume that the medium is anisotropic, the governing equation in the directions of anisotropic can be expressed as

$$k_{11}\frac{\partial^2 u}{\partial x_1^2}+2k_{12}\frac{\partial^2 u}{\partial x_1\partial x_2}+k_{22}\frac{\partial^2 u}{\partial x_2^2}=f(\boldsymbol{x}) \tag{1}$$

where k_{ij} is the coefficient of medium property. The fundamental solution of Eq. (1) is

$$u^*(\boldsymbol{x},\boldsymbol{y})=-\frac{1}{2\pi\sqrt{|D|}}\ln r(\boldsymbol{x},\boldsymbol{y}) \tag{2}$$

where

$$|D|=\begin{vmatrix}k_{11} & k_{12}\\ k_{12} & k_{22}\end{vmatrix}=k_{11}k_{22}-k_{12}^2\begin{bmatrix}s_{11} & s_{12}\\ s_{12} & s_{22}\end{bmatrix}=\frac{1}{|D|}\begin{bmatrix}k_{22} & -k_{12}\\ -k_{12} & k_{11}\end{bmatrix}$$

$$r(\boldsymbol{x},\boldsymbol{y})=\sqrt{s_{11}(x_1-y_1)^2+2s_{12}(x_1-y_1)(x_2-y_2)+s_{22}(x_2-y_2)^2}$$

Lemma 1. *Let $\psi(\boldsymbol{x})\in C^{0,\alpha}(\Gamma)$, and $\hat{\mathbf{x}}$ be a smooth point on Γ. For $\hat{\boldsymbol{x}}\in\Gamma$, taking the limit $\boldsymbol{y}\to\hat{\boldsymbol{x}}$, suppose $h=|\boldsymbol{y}-\hat{\boldsymbol{x}}|$ and $d=\inf_{x\in\Gamma}|\boldsymbol{y}-\boldsymbol{x}|$. If $h/d\le K_1$(with constant K_1), then there holds*

$$\lim_{\mathbf{y}\to\hat{\mathbf{x}}}\int_\Gamma\frac{x_k-y_k}{|\boldsymbol{x}-\boldsymbol{y}|^2}[\psi(\boldsymbol{x})-\psi(\hat{\boldsymbol{x}})]d\Gamma_x=\int_\Gamma\frac{x_k-\hat{x}_k}{|\boldsymbol{x}-\hat{\boldsymbol{x}}|^2}[\psi(\boldsymbol{x})-\psi(\hat{\boldsymbol{x}})]d\Gamma_x(k=1,2) \tag{3}$$

Proof. For the case that $k=1$, we will give the strict deduction here. The other can be performed in almost the same way.

For any $\varepsilon>0$, the difference between the left- and right-hand sides of Eq. (3) is

$$\Delta=\int_{\Gamma}\left[\frac{x_1-y_1}{|\boldsymbol{x}-\boldsymbol{y}|^2}-\frac{x_1-\hat{x}_1}{|\boldsymbol{x}-\hat{\boldsymbol{x}}|^2}\right][\psi(\boldsymbol{x})-\psi(\hat{\boldsymbol{x}})]d\Gamma_x$$

The integral Δ is divided into two parts: Δ_1 over $\Gamma_\delta=\{\boldsymbol{x}\in\Gamma\,|\,|\boldsymbol{x}-\hat{\boldsymbol{x}}|\le\delta\}$ and Δ_2 over $\Gamma_c=\Gamma-\Gamma_\delta$. First, we estimate Δ_1. Using $|y_k-\hat{x}_k|\le K_1|\boldsymbol{y}-\boldsymbol{x}|$, we have

$$\left|\frac{x_1-y_1}{|\boldsymbol{x}-\boldsymbol{y}|^2}-\frac{x_1-\hat{x}_1}{|\boldsymbol{x}-\hat{\boldsymbol{x}}|^2}\right|\le\frac{K_2}{|\boldsymbol{x}-\hat{\boldsymbol{x}}|}\quad\text{(with constant } K_2\text{)}$$

Besides, noting $\psi(\boldsymbol{x})\in C^{0,\alpha}(\Gamma)$, i.e., $|\psi(\boldsymbol{x})-\psi(\hat{\boldsymbol{x}})|\le K_3|\boldsymbol{x}-\hat{\boldsymbol{x}}|^{\alpha}$ (for constants α,K_3 with $0<\alpha\le1$), it yields $|\Delta_1|\le K_2K_3\int_{\Gamma_\delta}\frac{1}{|\boldsymbol{x}-\hat{\boldsymbol{x}}|^{1-\alpha}}d\Gamma_x$, and further $t=|\boldsymbol{x}-\hat{\boldsymbol{x}}|$denotes the bowstring corresponding to the arc $\overset{\frown}{x\hat{x}}$. Let $\hat{\boldsymbol{x}}$ be a smooth point on Γ. Hence, it is obvious that the ratio of the length of arc $\overset{\frown}{x\hat{x}}$ to that of bowstring t is bounded, i.e., $|d\Gamma_x|\le K_4dt$ (with constant K_4), therefore

$$|\Delta_1|\le K_2K_3K_4\int_0^{\delta}\frac{1}{t^{1-\alpha}}dt\le K_5\delta^{\alpha}\quad\left(K_5=\frac{1}{\alpha}K_2K_3K_4\quad\text{is a constant}\right)$$

By choosing sufficiently small δ, one has $|\Delta_1|\le\varepsilon/2$.

Now, we estimate Δ_2

$$|\Delta_2|\le\int_{\Gamma_c}\left|\frac{x_1-y_1}{(x_1-y_1)^2+(x_2-y_2)^2}-\frac{x_1-\hat{x}_1}{(x_1-\hat{x}_1)^2+(x_2-\hat{x}_2)^2}\right||\psi(\boldsymbol{x})-\psi(\hat{\boldsymbol{x}})|d\Gamma_x$$

Noting that δ has been fixed and $\hat{\boldsymbol{x}}$ does not belong to Γ_c, therefore by taking $|\boldsymbol{y}-\hat{\boldsymbol{x}}|$ sufficiently small it is obvious that $|\Delta_2|\le\varepsilon/2$. □

Lemma 2. *Consider the complete second order differential equation with variable coefficients*

$$L(u)=A\frac{\partial^2u}{\partial x_1^2}+2B\frac{\partial^2u}{\partial x_1\partial x_2}+C\frac{\partial^2u}{\partial x_2^2}+D\frac{\partial u}{\partial x_1}+E\frac{\partial u}{\partial x_2}+Fu=0$$

where $A,B,\ldots,F$ are given functions of x_1 and x_2 in Ω. Let us assume that $v(\boldsymbol{x})$ is twice continuously differentiable in Ω and once on Γ, we have

$$\int_{\Omega}[vL(u)-uL^*(v)]d\Omega=\int_{\Gamma}(Xn_1+Yn_2)d\Gamma\tag{4}$$

where

$$\mathrm{L}^*(v)=\frac{\partial^2(Av)}{\partial x_1^2}+2\frac{\partial^2(Bv)}{\partial x_1\partial x_2}+\frac{\partial^2(Cv)}{\partial x_2^2}-\frac{\partial(Dv)}{\partial x_1}-\frac{\partial(Ev)}{\partial x_2}+Fv$$

$$X=A\left(v\frac{\partial u}{\partial x_1}-u\frac{\partial v}{\partial x_1}\right)+B\left(v\frac{\partial u}{\partial x_2}-u\frac{\partial v}{\partial x_2}\right)+\left(D-\frac{\partial A}{\partial x_1}-\frac{\partial B}{\partial x_2}\right)uv$$

$$Y=B\left(v\frac{\partial u}{\partial x_1}-u\frac{\partial v}{\partial x_1}\right)+C\left(v\frac{\partial u}{\partial x_2}-u\frac{\partial v}{\partial x_2}\right)+\left(E-\frac{\partial B}{\partial x_1}-\frac{\partial C}{\partial x_2}\right)uv$$

Theorem 1. *Let Γ be a piecewise smooth curve. Then for the fundamental solution* (2)*, there holds*

$$\int_{\Gamma}\frac{\partial u^*(\boldsymbol{x},\boldsymbol{y})}{\partial\boldsymbol{m}_{\mathbf{x}}}d\Gamma=\begin{cases}-1, & \boldsymbol{y}\in\Omega\\ 0, & \boldsymbol{y}\in\Omega_c\end{cases},\int_{\Gamma}\frac{\partial u^*(\boldsymbol{x},\boldsymbol{y})}{\partial\boldsymbol{t}_{\mathbf{x}}}d\Gamma=0,\forall\boldsymbol{y}\in\Omega\cup\Omega_c\tag{5}$$

where

$$\boldsymbol{m}_{\boldsymbol{x}}=(k_{11}n_1(\boldsymbol{x})+k_{12}n_2(\boldsymbol{x}),k_{12}n_1(\boldsymbol{x})+k_{22}n_2(\boldsymbol{x}))^{\mathrm{T}},\boldsymbol{t}_{\boldsymbol{x}}=(t_1(\boldsymbol{x}),t_2(\boldsymbol{x}))^{\mathrm{T}}.$$

Proof. Letting $u=1,v=u^*$ in Lemma 2, we can obtain the first equation with $A=k_{11}$, $B=k_{12}$, $C=k_{22}$, $D=E=F=0$. The proof of the second equation can also be easily performed. □

3. Regularized indirect boundary integral equations

In this section, we will establish the regularized BIEs with indirect unknowns on Ω. The one on Ω_c is similar. The potential formulation on Ω can be written as

$$u(\boldsymbol{y})=\int_{\Gamma}\phi(\boldsymbol{x})u^*(\boldsymbol{x},\boldsymbol{y})d\Gamma+\int_{\Omega}f(\boldsymbol{x})u^*(\boldsymbol{x},\boldsymbol{y})d\Omega+C,\boldsymbol{y}\in\Omega\tag{6}$$

For any smooth point $\hat{\boldsymbol{x}}$ of Γ, by Theorem 1, we have

$$\begin{aligned}\nabla u(\boldsymbol{y})=&\int_{\Omega}f(\boldsymbol{x})\nabla u^*(\boldsymbol{x},\boldsymbol{y})d\Omega+\int_{\Gamma}[\phi(\boldsymbol{x})-\phi(\hat{\boldsymbol{x}})]\nabla u^*(\boldsymbol{x},\boldsymbol{y})d\Gamma+\phi(\hat{\boldsymbol{x}})\boldsymbol{g}(\hat{\boldsymbol{x}})\\&-\phi(\hat{\boldsymbol{x}})\int_{\Gamma}\left\{[\boldsymbol{g}(\boldsymbol{x})-\boldsymbol{g}(\hat{\boldsymbol{x}})]\frac{\partial u^*(\boldsymbol{x},\boldsymbol{y})}{\partial\boldsymbol{m}_{\mathbf{x}}}+[\boldsymbol{h}(\boldsymbol{x})-\boldsymbol{h}(\hat{\boldsymbol{x}})]\frac{\partial u^*(\boldsymbol{x},\boldsymbol{y})}{\partial\boldsymbol{t}_{\mathbf{x}}}\right\}d\Gamma\end{aligned}\tag{7}$$

where $\boldsymbol{g}(\boldsymbol{x})=(g_1(\boldsymbol{x}),g_2(\boldsymbol{x}))^{\mathrm{T}},\boldsymbol{h}(\boldsymbol{x})=(h_1(\boldsymbol{x}),h_2(\boldsymbol{x}))^{\mathrm{T}}$, and

$$g_i(\boldsymbol{x})=\frac{n_i(\boldsymbol{x})}{\Delta},h_i(\boldsymbol{x})=(-1)^{j-1}\frac{k_{1j}n_1(\boldsymbol{x})+k_{2j}n_2(\boldsymbol{x})}{\Delta}(i\ne j),$$
$$\Delta=k_{11}n_1^2(\boldsymbol{x})+2k_{12}n_1(\mathbf{x})n_2(\mathbf{x})+k_{22}n_2^2(\boldsymbol{x})$$

If $\hat{\boldsymbol{x}}\in\Gamma$ is a two-order smooth point, obviously $t_l(\boldsymbol{x})\in C^{0,\alpha}(\Gamma)$, $n_l(\boldsymbol{x})\in C^{0,\alpha}(\Gamma)(l=1,2)$, so there are $g_l(\boldsymbol{x})\in C^{0,\alpha}(\Gamma),h_l(\boldsymbol{x})\in C^{0,\alpha}(\Gamma)$ $(l=1,2)$. Therefore, as $\boldsymbol{y}\to\hat{\boldsymbol{x}}$, according to Lemma 1, we can immediately obtain the regularized BIEs with replacing $\hat{\boldsymbol{x}}$ by $\boldsymbol{y}$

$$\int_{\Gamma}\phi(\boldsymbol{x})d\Gamma+\int_{\Omega}f(\boldsymbol{x})d\Omega=0\tag{8}$$

$$u(\boldsymbol{y})=\int_{\Gamma}\phi(\boldsymbol{x})u^*(\boldsymbol{x},\boldsymbol{y})d\Gamma+\int_{\Omega}f(\boldsymbol{x})u^*(\boldsymbol{x},\boldsymbol{y})d\Omega+C,\boldsymbol{y}\in\Gamma\tag{9}$$

$$\begin{aligned}\nabla u(\boldsymbol{y})=&\phi(\boldsymbol{y})\boldsymbol{g}(\boldsymbol{y})+\int_{\Omega}f(\boldsymbol{x})\nabla u^*(\boldsymbol{x},\boldsymbol{y})d\Omega+\int_{\Gamma}[\phi(\boldsymbol{x})-\phi(\boldsymbol{y})]\nabla u^*(\boldsymbol{x},\boldsymbol{y})d\Gamma\\&-\phi(\boldsymbol{y})\int_{\Gamma}\left\{[\boldsymbol{g}(\boldsymbol{x})-\boldsymbol{g}(\boldsymbol{y})]\frac{\partial u^*(\boldsymbol{x},\boldsymbol{y})}{\partial\boldsymbol{m}_{\boldsymbol{x}}}+[\boldsymbol{h}(\boldsymbol{x})-\boldsymbol{h}(\boldsymbol{y})]\frac{\partial u^*(\mathbf{x},\mathbf{y})}{\partial\boldsymbol{t}_{\mathbf{x}}}\right\}d\Gamma\end{aligned}\tag{10}$$

Similarly, the regularized BIEs on Ω_c can be expressed as

$$\int_{\Gamma}\phi(\boldsymbol{x})d\Gamma+\int_{\Omega_c}f(\boldsymbol{x})d\Omega_c=0\tag{11}$$

$$u(\boldsymbol{y})=\int_{\Gamma}\phi(\boldsymbol{x})u^*(\boldsymbol{x},\boldsymbol{y})d\Gamma+\int_{\Omega_c}f(\boldsymbol{x})u^*(\boldsymbol{x},\boldsymbol{y})d\Omega_c+C,\boldsymbol{y}\in\Gamma\tag{12}$$

$$\begin{aligned}\nabla u(\boldsymbol{y})=&\int_{\Omega_c}f(\boldsymbol{x})\nabla u^*(\boldsymbol{x},\boldsymbol{y})d\Omega_c+\int_{\Gamma}[\phi(\boldsymbol{x})-\phi(\boldsymbol{y})]\nabla u^*(\boldsymbol{x},\boldsymbol{y})d\Gamma\\&-\phi(\boldsymbol{y})\int_{\Gamma}\left\{[\boldsymbol{g}(\boldsymbol{x})-\boldsymbol{g}(\boldsymbol{y})]\frac{\partial u^*(\boldsymbol{x},\boldsymbol{y})}{\partial\boldsymbol{m}_{\boldsymbol{x}}}+[\boldsymbol{h}(\boldsymbol{x})-\boldsymbol{h}(\boldsymbol{y})]\frac{\partial u^*(\boldsymbol{x},\boldsymbol{y})}{\partial\boldsymbol{t}_{\mathbf{x}}}\right\}d\Gamma\end{aligned}\tag{13}$$

Remark. If $\phi(\boldsymbol{x})\in C^{0,\alpha}(\Gamma),g_l(\hat{\boldsymbol{x}})\in C^{0,\alpha}(\Gamma),h_l(\hat{\boldsymbol{x}})\in C^{0,\alpha}(\Gamma)$ $(l=1,2)$, then the singularities of integrals in Eqs (10)and (13) should have been removed.

4. Numerical implementation

In this section, we shall perform the numerical integration strategy for Eqs. (9) and (10). The key problem is how to evaluate the integral when the field point is located at one of the nodes of the element under integration, while the other need not consider here because of involving only normal integrals.

4.1. Quadratic element

The boundary geometry is modeled by a continuous piecewise parabolic curve, while the distribution of the boundary quantity on each element is approximated by a discontinuous quadratic

element. Let $\psi^p(\xi)$ $(p=1,2,3)$ denote the shape function of quadratic Lagrange interpolation. i.e.

$$\psi^p(\xi)=\frac{(\xi/\alpha-\xi^q)(\xi/\alpha-\xi^r)}{(\xi^p-\xi^q)(\xi^p-\xi^r)} \quad \alpha\in(0,1] \quad (p,q,r=1,2,3;\ q\neq r;\ p\neq q,r)$$

where ξ is dimensionless coordinate and $\xi^k(k=p,q,r)$ represent the coordinate of node k. Let ξ and η denote the coordinate of source point $\boldsymbol{x}=(x_1,x_2)$ and field point $\boldsymbol{y}=(y_1,y_2)$, respectively, then there are

$$x_k=\sum_{p=1}^{3}\psi^p(\xi)x_k^p, y_k=\sum_{p=1}^{3}\psi^p(\eta)x_k^p, \text{ and } \frac{dx_k}{d\xi}=\sum_{p=1}^{3}\frac{d\psi^p(\xi)}{d\xi}x_k^p=\xi a_k+b_k$$

where $x_k^p(k=1,2;p=1,2,3)$ are node coordinates, and $a_k=\sum_{p=1}^{3}\frac{2x_k^p}{\xi^{pq}\xi^{pr}}, b_k=-\sum_{p=1}^{3}\frac{\xi^q+\xi^r}{\xi^{pq}\xi^{pr}}x_k^p$, with $\xi^{pq}=\xi^p-\xi^q$ and $(p,q,r=1,2,3;q\neq r,\ p\neq q,r)$, then

$$x_k-y_k=\rho\sum_{p=1}^{3}\boldsymbol{\Phi}^p(\xi,\eta)x_k^p \text{ and } \phi(\boldsymbol{x})-\phi(\boldsymbol{y})=\rho\sum_{p=1}^{3}\boldsymbol{\Phi}^p(\xi,\eta)\phi_k^p$$

where ρ and Φ^p are defined as

$$\rho=\xi-\eta, \boldsymbol{\Phi}^p(\xi,\eta)=\frac{\xi+\eta-\xi^q-\xi^r}{(\xi^p-\xi^q)(\xi^p-\xi^r)} (p\neq q,r;\ q\neq r)$$

besides

$$t_k(\boldsymbol{x})=\frac{1}{J(\xi)}\frac{dx_k}{d\xi}=\frac{\xi a_k+b_k}{J(\xi)}, n_k(\boldsymbol{x})=(-1)^{k+1}t_{k+1}(\boldsymbol{x}), t_k(\boldsymbol{y})=t_k(\boldsymbol{x})\big|_{\xi=\eta}, n_k(\boldsymbol{y})=n_k(\boldsymbol{x})\big|_{\xi=\eta}$$

with $J(\xi)=\sqrt{(dx_i/d\xi)(dx_i/d\xi)}$ and $(\cdot)_3=(\cdot)_1$, thus

$$t_k(\boldsymbol{x})-t_k(\boldsymbol{y})=\frac{\rho}{J(\xi)}U_k,\ n_k(\boldsymbol{x})-n_k(\boldsymbol{y})=\frac{(-1)^{k+1}\rho}{J(\xi)}U_{k+1} \tag{14}$$

where $U_k=\{a_k-(((\eta+\xi)a_ia_i+2a_ib_i)/(J(\eta)[J(\eta)+J(\xi)]))(\eta a_k+b_k)\}$, $k=1,2$, therefore

$$g_k(\boldsymbol{x})-g_k(\boldsymbol{y})=\frac{\rho}{\Delta_x\Delta_yJ(\xi)}\left\{\Delta_y(-1)^{k+1}U_{k+1}-(U_2V_1-U_1V_2)n_k(\boldsymbol{y})\right\} \tag{15}$$

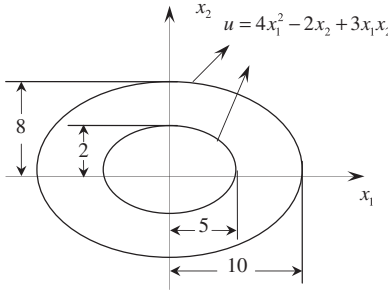

Fig. 1. Heat conduction in an elliptic cylinder.

$$h_k(\boldsymbol{x})-h_k(\boldsymbol{y})=(-1)^{k-1}\{k_{1k}[g_1(\boldsymbol{x})-g_1(\boldsymbol{y})]+k_{2k}[g_2(\boldsymbol{x})-g_2(\boldsymbol{y})]\} \tag{16}$$

with

$V_1=k_{11}[n_1(\boldsymbol{x})+n_1(\boldsymbol{y})]+2k_{12}n_2(\boldsymbol{x}), V_2=2k_{12}n_1(\boldsymbol{y})+k_{22}[n_2(\boldsymbol{x})+n_2(\boldsymbol{y})]$.

$\Delta_x=k_{11}n_1^2(\boldsymbol{x})+2k_{12}n_1(\boldsymbol{x})n_2(\boldsymbol{x})+k_{22}n_2^2(\boldsymbol{x})$,

$\Delta_y=k_{11}n_1^2(\boldsymbol{y})+2k_{12}n_1(\boldsymbol{y})n_2(\boldsymbol{y})+k_{22}n_2^2(\boldsymbol{y})$

Then, the singularities of the integrals in Eq. (10) should have been eliminated.

4.2. Exact element

In engineering applications, the structures with circle or ellipse boundaries are widely used in order to avoid stress concentrations around sharp corners. The elliptic arc elements are the extension of the circular arc elements, which can exactly depict these boundaries. For elliptic domain, its boundary geometric can be expressed as

$$x_1=a\cos\alpha_\xi, x_2=b\sin\alpha_\xi,\ \alpha_\xi=\frac{(1-\xi)}{2}\theta_1+\frac{(1+\xi)}{2}\theta_2, -1\le\xi\le1$$

we can arrive at

$$t_1(\boldsymbol{y})-t_1(\boldsymbol{x})=-(n_2(\boldsymbol{y})-n_2(\boldsymbol{x}))=\frac{a\beta}{J(\xi)}\sin\frac{\alpha_\eta-\alpha_\xi}{2}\cdot\left\{-\cos\gamma+\frac{\beta\sin\alpha_\eta}{2J(\eta)}\left[\frac{a^2\cos\gamma(\sin\alpha_\xi+\sin\alpha_\eta)}{J(\xi)+J(\eta)}-\frac{b^2\sin\gamma(\cos\alpha_\xi+\cos\alpha_\eta)}{J(\xi)+J(\eta)}\right]\right\}$$

$$t_2(\boldsymbol{y})-t_2(\boldsymbol{x})=n_1(\boldsymbol{y})-n_1(\boldsymbol{x})=\frac{b\beta}{J(\xi)}\sin\frac{\alpha_\eta-\alpha_\xi}{2}\cdot\left\{\sin\gamma+\frac{\beta\cos\alpha_\eta}{2J(\eta)}\left[\frac{a^2\cos\gamma(\sin\alpha_\xi+\sin\alpha_\eta)}{J(\xi)+J(\eta)}-\frac{b^2\sin\gamma(\cos\alpha_\xi+\cos\alpha_\eta)}{J(\xi)+J(\eta)}\right]\right\} \tag{17}$$

where $\beta=\theta_2-\theta_1, \gamma=((\alpha_\xi+\alpha_\eta)/2)$, and

$$\frac{\partial u^*(\mathbf{x},\mathbf{y})}{\partial y_j}=\frac{1}{\sin[(\alpha_\eta-\alpha_\xi)/2]}[\cdots], \quad (j=1,2) \tag{18}$$

The items $[\cdots]$ cannot lead to singular integral. According to the Eqs (17) and (18), the singularities of the integrals on the right side of Eq. (10) are eliminated.

5. Numerical examples

In this section, four examples of the anisotropic potential problems with curved boundaries are given to test the proposed method. The boundary geometry of the first three examples is depicted by the exact elements, while the last one by the linear elements.

Example 1. In this example, we consider the heat conduction in the elliptic cylinder with the thermal conductivity tensor k_{ij} given by $k_{11}=1$, $k_{12}=2$, $k_{22}=5$, and the analytical temperature distribution and the values of semi-major and semi-minor axes shown in Fig. 1.

Table 1
The numerical results of temperatures at internal points in the elliptic cylinder.

Internal points(y_1,y_2)		Exact	Present	Relative error (%)
0.6000000E+01	0.0000000E+00	0.1520000E+03	0.1520003E+03	−0.2008555E−03
0.4242641E+01	0.2828427E+01	0.1000000E+03	0.9999542E+02	0.4580355E−02
0.3673819E−15	0.4000000E+01	−0.2400000E+02	−0.2399474E+02	0.2192336E−01
−0.4242641E+01	0.2828427E+01	0.2800000E+02	0.2799787E+02	0.7595139E−02
−0.6000000E+01	0.4898425E−15	0.1520000E+03	0.1520003E+03	−0.2008555E−03
−0.4242641E+01	−0.2828427E+01	0.1000000E+03	0.9999542E+02	0.4580355E−02
−0.1102146E−14	−0.4000000E+01	−0.2400000E+02	−0.2399474E+02	0.2192336E−01
0.4242641E+01	−0.2828427E+01	0.2800000E+02	0.2799787E+02	0.7595139E−02

There are 30 exact elements divided along the whole boundaries, 6 equally spaced elements over inner boundary, and 24 equally spaced elements over outer boundary. Quadratic discontinuous interpolation is adopted to approximate the boundary functions.

The numerical results of temperatures at internal points are presented in Table 1 in comparison with the exact solution, together with the relative errors (%). It can be seen that compared with the exact solution, the present results are satisfactory despite using small computational element numbers. In order to further show the efficiency, Fig. 3 depicts the convergence curve of the internal point (0,4), whose computational accuracy is somewhat inferior to others. From the steep slope of the curve in Fig. 3 it is shown that the convergence speed is quite fast with increase of the number of boundary elements.

Tables 2 and 3 list the numerical results of gradients $\partial u/\partial x$ and $\partial u/\partial y$ on partial boundary ($0 \sim \pi/2$), respectively. It may easily be concluded from these two tables that the proposed method can produce highly accurate numerical solutions. With the increase of the discretized boundary elements, the maximum relative errors (%)

Table 2
The numerical results of $\partial u/\partial x$ at the boundary points in the elliptic cylinder.

Boundary points (θ)	Exact	Present	Relative error (%)
Inner boundary			
0	0.4000000E+02	0.4000209E+02	−0.5214306E−02
$\pi/12$	0.3708412E+02	0.3707576E+02	0.2254886E−01
$\pi/6$	0.3164102E+02	0.3164111E+02	−0.2942148E−03
$\pi/4$	0.2404163E+02	0.2404251E+02	−0.3657422E−02
$\pi/3$	0.4557207E+01	0.4550338E+01	0.1507150E+00
$\pi/2$	0.6000000E+01	0.5990033E+01	0.1661165E+00
Outer boundary			
0	0.8000000E+02	0.7989933E+02	0.1258357E+00
$\pi/24$	0.8244822E+02	0.8238517E+02	0.7647303E−01
$\pi/8$	0.8309476E+02	0.8308516E+02	0.1156012E−01
$5\pi/24$	0.7807854E+02	0.7811147E+02	−0.4217532E−01
$7\pi/24$	0.6774139E+02	0.6780300E+02	−0.9093795E−01
$3\pi/8$	0.5278778E+02	0.5286013E+02	−0.1370609E+00
$11\pi/24$	0.3423677E+02	0.3430139E+02	−0.1887300E+00
$\pi/2$	0.2400000E+02	0.2405394E+02	−0.2247462E+00

Table 3
The numerical results of $\partial u/\partial y$ at boundary points in the elliptic cylinder.

Boundary points (θ)	Exact	Present	Relative error (%)
Inner boundary			
0	0.1500000E+02	0.1500215E+02	−0.1436635E−01
$\pi/12$	0.1655944E+02	0.1656417E+02	−0.2857082E−01
$\pi/6$	0.1699038E+02	0.1699091E+02	−0.3130678E−02
$\pi/4$	0.1626346E+02	0.1626227E+02	0.7296392E−02
$\pi/3$	0.1160969E+02	0.1161332E+02	−0.3120835E−01
$\pi/2$	−0.8000000E+01	−0.7994361E+01	0.7048955E−01
Outer boundary			
0	0.3000000E+02	0.3005437E+02	−0.1812400E+00
$\pi/24$	0.2556651E+02	0.2559953E+02	−0.1291765E+00
$\pi/8$	0.1547052E+02	0.1547745E+02	−0.4480547E−01
$5\pi/24$	0.4320234E+01	0.4308057E+01	0.2818686E+00
$7\pi/24$	−0.7124464E+01	−0.7149434E+01	−0.3504840E+00
$3\pi/8$	−0.1808364E+02	−0.1811451E+02	−0.1706723E+00
$11\pi/24$	−0.2781045E+02	−0.2783755E+02	−0.9744332E−01
$\pi/2$	−0.3200000E+02	−0.3202299E+02	−0.7183424E−01

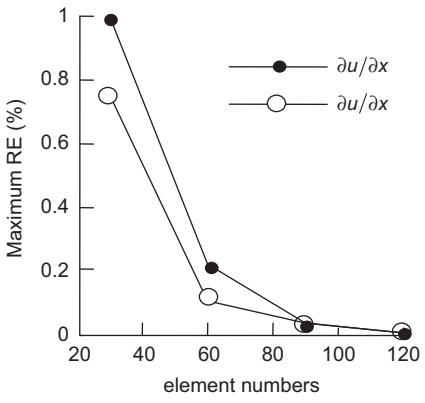

Fig. 2. Convergence curves of $\partial u/\partial x$ and $\partial u/\partial y$.

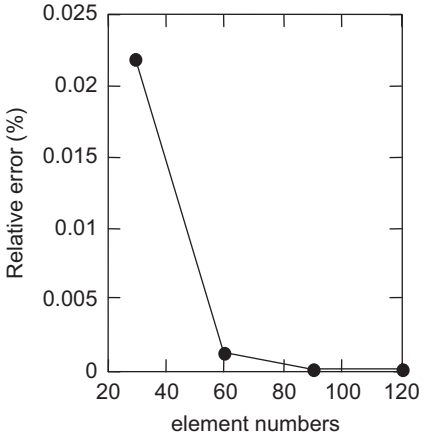

Fig. 3. Convergence curves of temperature at interior points.

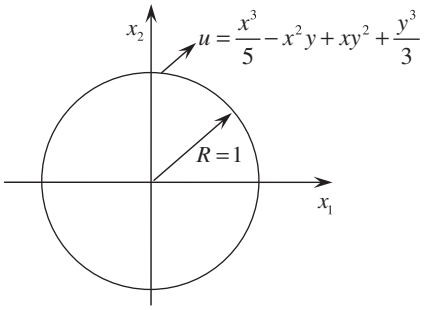

Fig. 4. Boundary conditions of Example 2.

Table 4
The comparison between the current method and existing method.

N	Analytical solution	Numerical solution	Relative error (%)
(a) DLBEM			
40	0.008333	0.008244	1.071
60	0.008333	0.008288	0.544
80	0.008333	0.008308	0.298
(b) QBEM			
40	0.008333	0.008261	0.863
60	0.008333	0.008314	0.237
80	0.008333	0.008325	0.099
(c) DQBEM			
40	0.008333	0.008333	0.009
60	0.008333	0.008333	0.002
80	0.008333	0.008333	0.001
(d) Present method			
40	0.8333333E−02	0.8333000E−02	0.3997477E−02
60	0.8333333E−02	0.8333292E−02	0.5005535E−03
80	0.8333333E−02	0.8333328E−02	0.6566266E−04

Table 5
The numerical results of temperatures at internal points with $N=40$.

Internal points (y_1, y_2)		Exact	Present	Relative error (%)
0.3061516E−16	−0.5000000E+00	−0.4166667E−01	−0.4166683E−01	−0.3939381E−03
0.4330127E+00	−0.2500000E+00	0.8496794E−01	0.8496739E−01	0.6463444E−03
0.4330127E+00	0.2500000E+00	0.1634604E−02	0.1633924E−02	0.4154949E−01
0.3061516E−16	0.5000000E+00	0.4166667E−01	0.4166683E−01	−0.3939381E−03
−0.4330127E+00	0.2500000E+00	−0.8496794E−01	−0.8496739E−01	0.6463444E−03
−0.4330127E+00	−0.2500000E+00	−0.1634604E−02	−0.1633924E−02	0.4154949E−01

Table 6
The numerical results of flux at boundary points with $N=40$.

Boundary points (y_1, y_2)		Exact	Present	Relative error (%)
0.9969173E+00	0.7845910E−01	0.5706522E+00	0.5705870E+00	0.1142973E−01
0.9238795E+00	0.3826834E+00	−0.2613126E+00	−0.2614194E+00	−0.4085647E−01
0.8314696E+00	0.5555702E+00	0.1447581E+00	0.1454666E+00	−0.4894102E+00
0.6788007E+00	0.7343225E+00	0.1368370E+01	0.1367303E+01	0.7792549E−01
0.4886212E+00	0.8724960E+00	0.2760840E+01	0.2761706E+01	−0.3138780E−01
0.3461171E+00	0.9381913E+00	0.3390250E+01	0.3390674E+01	−0.1250639E−01
0.2334454E+00	0.9723699E+00	0.3567128E+01	0.3567247E+01	−0.3341742E−02
0.1950903E+00	0.9807853E+00	0.3559612E+01	0.3559451E+01	0.4540198E−02

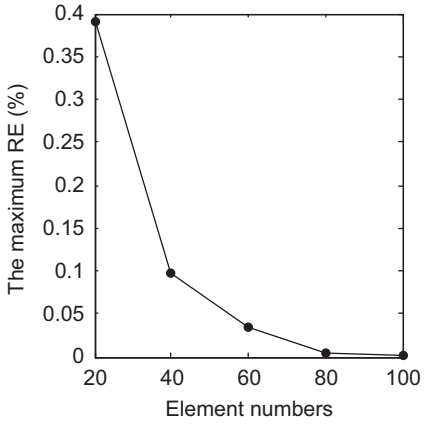

Fig. 5. Maximum RE (%) of flux at boundary points changes with the increase of element numbers.

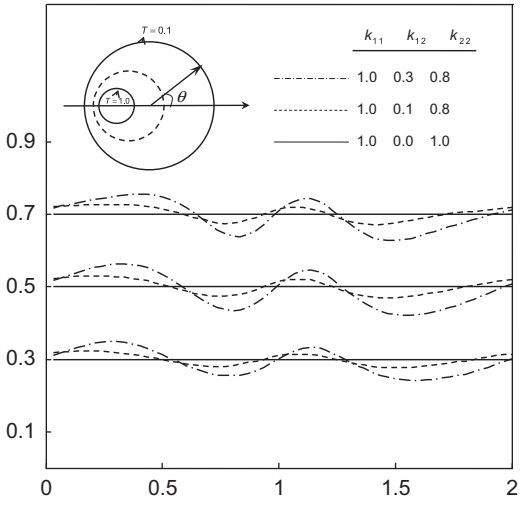

Fig. 6. Temperature distribution in anisotropic and isotropic media for various values of k_{12}.

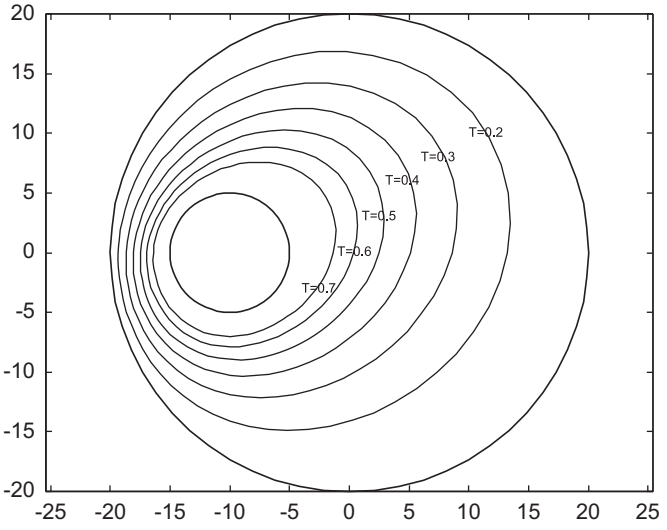

Fig. 7. Isotherm distribution with $k_{11}=1.0$, $k_{12}=0.3$, $k_{22}=0.8$.

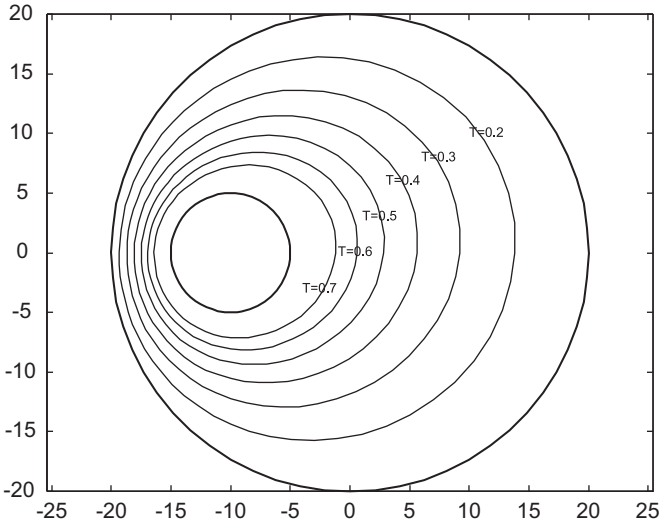

Fig. 8. Isotherm distribution with $k_{11}=1.0$, $k_{12}=0.1$, $k_{22}=0.8$.

of gradients at the boundary points are depicted in Fig. 2, from which we can observe that the convergence speeds of the computed gradients are fast.

Example 2. We consider the heat conduction of an anisotropic medium with the thermal conductivity tensor k_{ij} given by $k_{11}=5$, $k_{12}=2$, $k_{22}=1$. The analytical temperature distribution can be seen in Fig. 4.

This problem is solved in the plane domain $\Omega=\{(x,y): x^2+y^2<1\}$. In order to demonstrate the better precision and high computational efficiency, a comparison between the current method and existing method [32] is presented in Table 4. The numerical results of DLBEM, QBEM and DQBEM with various numbers of boundary element $N\in\{40,60,80\}$are obtained from Re [32] at internal point (0.25,0.25). Besides, we also calculate temperatures at more internal points and flux at boundary points to show the universality and improvement of current technique, which are listed in Tables 5 and 6, respectively. Fig. 5 depicts that with the increase of the discretized boundary elements, the maximum relative errors (RE) (%) of flux at boundary points change, from which we can see that the convergence rates of the present method are fast.

Example 3. [38] In order to test how the thermal conductivity tensors k_{ij} influence the temperature distribution, here we consider a hollow eccentric cylinder whose inner and outer radii are 5 and 20, respectively, as shown in Fig. 6. The center of the inner circle is located at point $(-10,0)$. For the hollow cylinder, uniform and constant temperatures are assumed at the inner and outer surfaces.

For various values of k_{12}, Fig. 6 depicts the temperature distribution in anisotropic and isotropic media. It is worth noting that the most significant quantity to characterize the anisotropy of a media is the determinant of the conductivity coefficients, i.e. $|k_{ij}|=k_{11}k_{22}-k_{12}^2$. The smaller is the value of $|k_{ij}|$, the more asymmetric are the temperature fields. Figs. 7 and 8 show the isotherm distribution of the eccentric cylinder with two different conductivity coefficients, respectively.

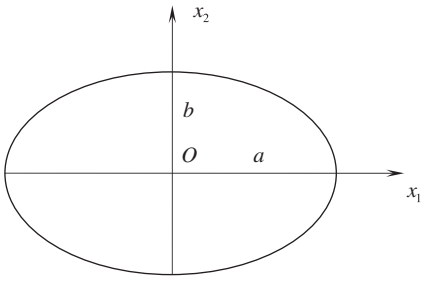

Fig. 9. A bar with elliptic cross section.

Example 4. An anisotropic bar with elliptic cross section subjected to the pure torque on the end surface, is considered in this example, as shown in Fig. 9. The semi-axes of the ellipse are $a=10$ and $b=5$, and the ratio of stiffness coefficients is chosen as $k_{11}/k_{22}=4$ and $k_{12}/k_{22}=0.2$.

Considering the torsion of anisotropic uniform bar, the regularized BIEs for computing the shear stress components can be easily derived by using the following relation and combining the Eqs. (10)

$$\begin{Bmatrix}\tau_{yz}\\ \tau_{xz}\end{Bmatrix}=\theta\begin{bmatrix}k_{22} & k_{12}\\ k_{12} & k_{11}\end{bmatrix}\left[\frac{\partial u}{\partial x_2}+x_1 \quad \frac{\partial u}{\partial x_1}-x_2\right]^{\mathrm{T}}$$

where u represents the torsion function and θ is the twist angle of unit length in axial direction of the bar.

There are 24 exact elements divided along the whole boundaries, while quadratic discontinuous interpolation, i.e. discontinuous element, is adopted to approximate the boundary functions. The numerical results of the shear stresses τ_{xz}/θ, τ_{yz}/θ of boundary and internal points (as $a'=5, b'=2.5$) are listed in Tables 7 and 8, respectively, from which it can be seen that compared with the exact solution, the present results are in good agreement with the exact solutions.

Example 5. [38] Flow under dam with two different orthotropic soils is considered. The soil in the lower layer is anisotropic with $k'_{11}=0.25\times10^{-5}$ m/s and$k'_{22}=0.075\times10^{-5}$ m/s; the principal permeability of the upper stratum makes an angle of 45° with the horizontal and their coefficients of permeability $k_{11}=4.0\times10^{-5}$ m/s and $k_{22}=1.0\times10^{-5}$ m/s. The dam retains 20 m of water upstream and has 5 m of tail water downstream.

There are 48 linear elements divided along the boundary of the upper dam, meanwhile 44 linear elements for the boundary of the down dam. Fig. 10 gives the pressure distribution on the dam base, the equipotent lines at various points under the dam.

6. Conclusions

A novel regularization technique, in which the nonsingular IBIE excluding the CPV and HFP integrals is established, is pursued for the homogeneous anisotropic potential problems. With the proposed algorithm, the considered problems are solved directly with no inverse transformation, and fairly high accuracy of numerical results is achieved. Furthermore, this method does

Table 7
The numerical results of shear stresses at the boundary points.

Boundary points		Present	Exact	Relative error (%)
x_1	x_2	$\tau_{xz}(\tau_{yz})/\theta$	$\tau_{xz}(\tau_{yz})/\theta$	τ_{xz}/θ
0.9978589E+01	0.3270156E+00	−0.6507096E+00(0.4963955E+01)	−0.6507529E+00(0.4964285E+01)	0.6654281E−02
0.9807853E+01	0.9754516E+00	−0.1941006E+01(0.4879048E+01)	−0.1941124E+01(0.4879345E+01)	0.6087608E−02
0.9469301E+01	0.1607197E+01	−0.3198248E+01(0.4710868E+01)	−0.3198282E+01(0.4710918E+01)	0.1065573E−02
0.8968727E+01	0.2211443E+01	−0.4400637E+01(0.4461804E+01)	−0.4400717E+01(0.4461886E+01)	−0.1824933E−02
0.8314696E+01	0.2777851E+01	−0.5527991E+01(0.4136612E+01)	−0.5527854E+01(0.4136509E+01)	−0.2482399E−02
0.7518398E+01	0.3296729E+01	−0.6560543E+01(0.3740433E+01)	−0.6560408E+01(0.3740356E+01)	−0.2063332E−02
0.6593458E+01	0.3759199E+01	−0.7480848E+01(0.3280264E+01)	−0.7480712E+01(0.3280204E+01)	−0.1823557E−02
0.5555702E+01	0.4157348E+01	−0.8273186E+01(0.2763983E+01)	−0.8273018E+01(0.2763927E+01)	−0.2032222E−02
0.4422887E+01	0.4484364E+01	−0.8923858E+01(0.2200380E+01)	−0.8923771E+01(0.2200358E+01)	−0.9696586E−03
0.3214395E+01	0.4734651E+01	−0.9421958E+01(0.1599162E+01)	−0.9421836E+01(0.1599141E+01)	−0.1299152E−02
0.1950903E+01	0.4903926E+01	−0.9758712E+01(0.9705643E+00)	−0.9758690E+01(0.9705621E+00)	−0.2246123E−03
0.6540313E+00	0.4989295E+01	−0.9928625E+01(0.3253782E+00)	−0.9928571E+01(0.3253765E+00)	−0.5408201E−03

Table 8
The numerical results of shear stresses at internal points.

Internal points	Present		Exact		Relative error (%)	
θ	τ_{yz}/θ	τ_{xz}/θ	τ_{yz}/θ	τ_{xz}/θ	τ_{yz}/θ	τ_{xz}/θ
$\pi/10$	0.2365719E+01	−0.1537349E+01	0.2365723E+01	−0.1537340E+01	0.1669092E−03	−0.5562902E−03
$\pi/5$	0.2012404E+01	−0.2924209E+01	0.2012404E+01	−0.2924195E+01	0.1321292E−04	−0.4762715E−03
$3\pi/10$	0.1462101E+01	−0.4024820E+01	0.1462097E+01	−0.4024809E+01	−0.2693607E−03	−0.2694455E−03
$2\pi/5$	0.7686761E+00	−0.4731451E+01	0.7686701E+00	−0.4731446E+01	−0.7833488E−03	−0.1035127E−03
$3\pi/5$	−0.7686639E+00	−0.4731441E+01	−0.7686701E+00	−0.4731446E+01	0.7977797E−03	0.1234607E−03
$7\pi/10$	−0.1462093E+01	−0.4024799E+01	−0.1462097E+01	−0.4024809E+01	0.2945465E−03	0.2508246E−03
$4\pi/5$	−0.2012403E+01	−0.2924184E+01	−0.2012404E+01	−0.2924195E+01	0.4512591E−04	0.3521772E−03
$9\pi/10$	−0.2365724E+01	−0.1537336E+01	−0.2365723E+01	−0.1537340E+01	−0.4505264E−04	0.2421450E−03

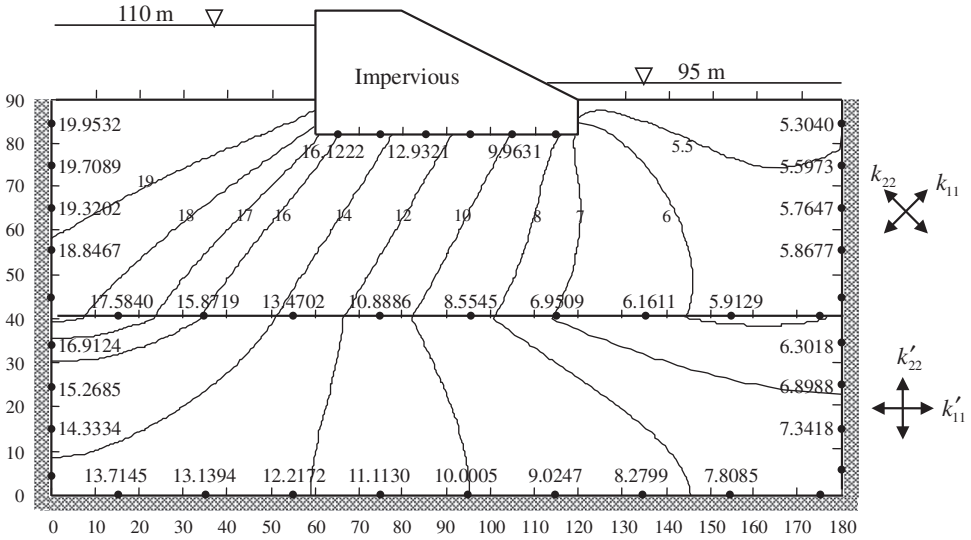

Fig. 10. Seepage flow under dam with two different orthotropic soils.

not need to calculate multiple integral as the Galerkin method, but rather treat CPV integrals indirectly, so it is simple and easy for programming. Also, our numerical experiments indicate that, from the point of view of numerical accuracy, the proposed method is superior over the stand BEM using direct formulations, especially for solving some particular examples such as contact problems, sensitivity problems, and the study of thin bodies. In addition, although the boundary unknown physical quantities cannot be obtained directly by using the proposed method which is based on the indirect boundary integral equations, the total computational costs are not as high as expected compared to the costs associated with the direct BEM because no difficult hypersingular integrals need to treat in the indirect method.

Acknowledgements

The support from the National Natural Science Foundation of China (10571110), the Opening Fund of the State Key Laboratory of Structural Analysis for Industrial Equipment (GZ1017) and the National Natural Science Foundation of Shangdong Province of China (ZR2010AZ003) are gratefully acknowledged.

References

[1] Tanaka M, Sladek V, Sladek J. Regularization techniques applied to boundary element methods. Appl Mech Rev 1994;47:457–99.
[2] Toh KC, Mukherjee S. Hypersingular and finite part integrals in the boundary element method. Int J Solids Struct 1994;31:2299–312.
[3] Sun HC, et al. Nonsingular boundary element method. Dalian: Dalian University of Technology Press; 1999. (in Chinese).
[4] Sladek V, Sladek J, Tanaka M. Regularization of hypersingular and nearly singular integrals in the potential theory and elasticity. Int J Numer Meth Eng 1993;36:1609–28.
[5] John W, Tsay TK. Analytical evaluation and application of the singularities in boundary element method. Eng Anal Bound Elem 2005;29:241–56.
[6] Padhi GS, Shenoi RA, Moy SSJ, et al. Analytical Integration of kernel shape function product integrals in the boundary element method. Comput Struct 2001;79:1325–33.
[7] Lifeng M A, Korsunsky Alexander M. A note on the Gauss–Jacobi quadrature formulae for singular integral equations of the second kind. Int J Fract 2004;126:339–405.
[8] Huber O, Lang A, Kuhn G. Evaluation of the stress tensor in 3D elastostatics by direct solving of hypersingular integrals. Comput Mech 1993;12:39–50.
[9] Karami G, Derakhshan D. An efficient method to evaluate hypersingular and supersingular integrals in boundary integral equations analysis. Eng Anal Boundary Elem 1999;23:317–26.
[10] Telles JCF. A self-adaptive co-ordinate transformation for efficient numerical evaluation of general boundary element integrals. Int J Numer Methods Eng 1987;24:959–73.
[11] Cerrolaza M, Alarcón E. A bi-cubic transformation for the numerical evaluation of the Cauchy principal value integrals in boundary methods. Int J Numer Methods Eng 1989;28:987–99.
[12] Niu ZR, Zhou HL. A novel boundary integral integral equation method for linear elasticity-natural boundary integral equation. ACTA Mech Solida Sin 2001;14:1–10.
[13] Kutt HR. The numerical evaluation of principal value integrals by finite-part integration. Numer Math 1975;24:205–10.
[14] Kutt HR, Quadrature formulae for finite-part integrals, Technical Report CSIR Special Report WISK 178, National Research Institute for Mathematical Sciences, CSIR, South Africa; 1975.
[15] Dominguez, et al. Flux and traction boundary elements without hypersingular or singular integrals. Int J Numer Methods Eng 2000;48:111–35.
[16] Jorge, et al. Self regular boundary integral equation formulations for Laplace's equation in 2-D. Int J Numer Methods Eng 2001;51:1–29.

[17] Guiggiani M, Casalini P. Direct computation of Cauchy principal value integrals in advanced boundary elements. Int J Number Methods Eng 1987;24:1711–20.
[18] Guiggiani M, Krishnasamy G, Rudolphi TJ, et al. General algorithm for the numerical solution of hyper-singular boundary integral equations. (ASME) J Appl Mech 1992;59:604–14.
[19] Gao XW, Yang K, Wang J. An adaptive element subdivision technique for evaluation of various 2D singular boundary integrals. Eng Anal Boundary Elem 2008;32:692–6.
[20] Gao XW. Numerical evaluation of two-dimensional boundary integrals—theory and Fortran code singular. J Comput Appl Math 2006;188:44–64.
[21] Zhang YM, Sun HC. Analytical treatment of boundary integrals in direct boundary element analysis of plan potential and elasticity problems. Appl Math Mech 2001;22:593–601. [in Chinese].
[22] Zhang YM, Sun HC. Theoretic analysis on virtual boundary element. Chin J Comput Mech 2000;17:56–62. [in Chinese].
[23] Chen JT, Shen WC, Chen PY. Analysis of circular torsion bar with circular holes using null-field approach. Comput Modelling Eng Sci 2006;12:109–19.
[24] Chen JT, Shen WC, Wu AC. Null-field integral equations for stress field around circular holes under antiplane shear. Eng Anal Boundary Elem 2006;30:205–17.
[25] Chen JT, Hsiao CC, Leu SY. Null-field integral equation approach for plate problems with circular boundaries. ASME J Appl Mech 2006;73:619–93.
[26] Liu YJ. On the simple solution and non-singular nature of the BIE/BEM-a review and some new results. Eng Anal Bound Elem 2000;24:286–92.
[27] Rudolphi TJ. Higher order elements and element enhancement by combined regular and hypersingular boundary integral equations. Boundary Elem Methods Eng 1990:448–55.
[28] Hu HC. Analogy between anti-plane shear waves in anisotropic and isotropic media. Acta Mech Solida Sin 1991;12:261–4. [in Chinese].
[29] Rungamornrat Jaroon, Wheeler Mary F. Weakly singular integral equations for Darcy's flow in anisotropic porous media. Eng Anal Bound Elem 2006;30:237–46.
[30] Rungamornrat Jaroon. Modeling of flow in three-dimensional, multi-zone, anisotropic porous media with weakly singular integral equation method. J Eng Mech 2009;135:828–38.
[31] Wang YB, Sun YZ. A new boundary integral equation method for cracked 2-D anisotropic bodies. Eng Frac Mech 2005;72:2128–43.
[32] Mera NS, Elliott L, Ingham DB, et al. A comparison of boundary element method formulations for steady state anisotropic heat conduction problems. Eng Anal Boundary Elem 2001;25:115–28.
[33] Mera NS, Elliott L, Ingham DB, et al. The boundary element solution of the Cauchy steady heat conduction problem in an anisotropic medium. Int J Numer Methods Eng 2000;49:481–99.
[34] Wu CP, Lin CH, Chiou YJ. Multi-region boundary element analysis of unconfined seepage problems in excavations. Comput Geotechnics 1996;19:75–96.
[35] Brebbia CA, Chang OV. Boundary elements applied to seepage problems in zoned anisotropic Soils, MSc thesis, Southampton University; 1979.
[36] Dumir PC, Kumar R. Complex variable boundary element method for torsion of anisotropic bars. Appl Math Modelling 1993;17:80–8.
[37] Chen JT, Hong HK, Chyuan SW. Boundary element analysis and design in seepage problems using dual integral formulation. Finite Elem Anal Design 1994;17:1–20.
[38] Brebbia CA, Telles JCF, Wrobel LC. Boundary element techniques: theory and application in engineering. Springer-Verlag; 1984 p. 108–10.